

New scaling measurements map the transition from single-particle to correlated-pair dominance in atomic nuclei

I. Korover,^{1,*} A.W. Denniston,^{1,*} A. Schmidt,² A. Kiral,¹ A. Lovato,³ N. Rocco,⁴ L.B. Weinstein,⁵ E. Piasetzky,⁶ O. Hen,^{1,†} and the CLAS Collaboration

¹*Massachusetts Institute of Technology, Cambridge, Massachusetts 02139, USA*

²*The George Washington University, Washington DC 20052, USA*

³*Physics Division, Argonne National Laboratory, Lemont, Illinois 60439, USA*

⁴*Theoretical Physics Department, Fermi National Accelerator Laboratory, P.O. Box 500, Batavia, Illinois 60510, USA*

⁵*Old Dominion University, Norfolk, Virginia 23529, USA*

⁶*School of Physics and Astronomy, Tel Aviv University, Tel Aviv 69978, Israel*

The structure and properties of atomic nuclei result from the many-body interactions between their constituent nucleons (protons and neutrons). Nucleons with momenta below the nuclear Fermi momentum are well modeled as independent particles moving in an average mean field [1–3]. Above it, they are predominantly part of strongly-interacting short-range correlated pairs [4–6]. Understanding the transition between these two distinct regimes is an outstanding challenge. Here we report on observations of a new kind of scaling in the electron scattering cross-section ratio for nuclei relative to deuterium. Detecting both the scattered electron and knocked-out proton, we study the scaling onset dependence on initial nucleon momentum. We find the independent particle to correlated-pair transition occurs just above the nuclear Fermi momentum, with a narrow transition width of approximately 10% of the Fermi momentum. The narrow transition width supports the factorization of the many-body nuclear wave-function to a low-momentum single-particle region and a high-momentum correlated-pair region [5, 7–9]. This allows constructing precise effective nuclear wave functions and spectral functions that can improve our understanding of the fundamental structure of matter [10, 11], and neutrino-nucleus interactions for precision neutrino oscillation measurements [12].

Traditional effective mean-field nuclear models simplify the calculation of nuclear wave functions by averaging over the effects of the individual nucleon-nucleon (NN) interactions to determine effective single-nucleon potentials. These potentials give rise to nuclear shell-model states, e.g. s -, p -, d -, ... shells, with typical nucleon momenta in each shell below the nuclear Fermi momentum (k_F). Measured Fermi momenta for medium to heavy nuclei range from $k_F = 220$ MeV/c in carbon to 260 MeV/c in lead [37].

When two nucleons get close to each other, the very strong short-range NN interaction becomes much larger than the average nuclear mean-field. This temporal fluctuation of high local nucleon density is known as a short range correlated (SRC) nucleon pair [4–6, 13]. Nucleons in SRC pairs have high relative momentum, greater than k_F , and thus populate states at higher momenta than that of shell model states. Since the short-range NN interaction is the same in all nuclei, the properties of SRC pairs are universal, i.e., largely the same for all nuclei [5, 9].

The formation of SRCs depletes the occupancy of shell model states and introduces a high-momentum “tail” ($k > k_F$) to the nuclear momentum distribution [5, 13, 14]. Thus, a complete microscopic description of atomic nuclei must go beyond the nuclear shell-model and account for both the mean-field effects nucleons experience when they are relatively far apart and the explicit strong correlation effects they experience at short distances.

Effective theoretical models of nuclei can combine nucleus-dependent mean-field momentum distributions with the universal properties of SRC pairs [5, 15–17]. Such models well describe the high- and low-momentum regimes (and the equivalent short- and long-ranged regimes) of the many-body nuclear distribution [9, 18]. However, the transition between the two regimes is still not well understood, which limits their applicability.

Here we map the mean-field to SRC regime transition using new measurements of high-energy electron scattering. We observe a new type of scaling in the cross-section ratio for nuclei relative to deuterium, that extends over a much broader kinematic range than previous measurements. By accounting for residual mean-field contributions, we isolate the SRC response function and observe a narrow mean-field to SRC transition at slightly more than k_F .

Our experiment ran at the Thomas Jefferson National Accelerator Facility. It used a 5.01 GeV unpolarized electron beam incident on a dedicated target system consisting of a deuterium cell followed by an interchangeable solid foil of Carbon (C), Aluminum (Al), Iron (Fe), or Lead (Pb) [19]. Scattered electrons and knocked-out protons were identified and measured using the CEBAF Large Acceptance Spectrometer (CLAS) [20]. See Methods for details.

In high-energy quasi-elastic (QE) scattering, the electron scatters by exchanging a single virtual photon with momentum \vec{q} and energy ω that is absorbed by a single nucleon which gets knocked-out of the nucleus with momentum \vec{p}_p . By measuring both the scattered electron and knocked-out proton, i.e. the $(e, e'p)$ reaction, we can determine the missing momentum $\vec{p}_{miss} = \vec{p}_p - \vec{q}$ and energy $E_{miss} = \sqrt{(p_p^2 + m_p^2)} - \omega$ of the reaction. If the knocked-out nucleon does not re-interact as it leaves the nucleus, \vec{p}_{miss} and E_{miss} are equal to the initial momentum and energy of that nucleon.

In a high-resolution reaction picture we expect the reaction to be sensitive to mean-field nucleons at low- p_{miss} and to SRCs at high- p_{miss} [21]. In the SRC dominated region, the cross-section ratio for any two nuclei should be constant (equal to the relative number of high-momentum nucleons in the two nuclei). Thus, by measuring the $(e, e'p)$ cross-section ratio for nuclei relative to deuterium for different minimum p_{miss} , we can look for the onset of scaling that corresponds to SRC pair dominance in the nuclear momentum distribution.

Previous scaling studies used measurements of inclusive (e, e') reactions where only the scattered electron is detected [15, 22–25]. Here the momentum transfer $Q^2 = q^2 - \omega^2$ and Bjorken scaling parameter $x_B = \frac{Q^2}{2m\omega}$ (where m is the nucleon mass) can be related to the minimal allowed initial momentum for the struck nucleon in the nucleus, assuming quasi-free (QF) scattering from either single nucleons or from nucleons in an SRC pair at rest. In addition, choosing $x_B > 1$ also reduces the contribution from non-quasi-elastic scattering, where the electron can scatter from a pion exchanged between two nucleons or can excite the struck nucleon to a resonance.

For $Q^2 \geq 1.5 \text{ GeV}/c^2$, the cross section ratio of nuclei to deuterium is constant for $1.5 \leq x_B \leq 2$ [15, 22–25], a phenomena we call scaling (see Figs. 1 and 2). This scaling occurs because at these values of Q^2 and x_B the electron can only scatter off nucleons with momentum greater than k_F , i.e., only nucleons in SRC pairs [15, 22]. The universality of SRC pairs makes the cross-section scale and the average cross-section ratio for any nucleus relative to deuterium is interpreted as a measure of the relative number of nucleons in SRC pairs in the measured nuclei.

However, recent studies [26] show that the relation between Q^2 , x_B and the minimal initial nucleon momentum also depends on the detailed characteristics of SRC pairs such as their center-of-mass motion and the excitation energy of the residual nuclear system. This prevents a precise determination of the SRC scaling onset from the high- x_B (e, e') scaling measurements.

In contrast, the $(e, e'p)$ reaction used in this paper is insensitive to such model details because detecting the proton allows us to directly determine \vec{p}_{miss} for each event, thereby enabling a complementary and precise determi-

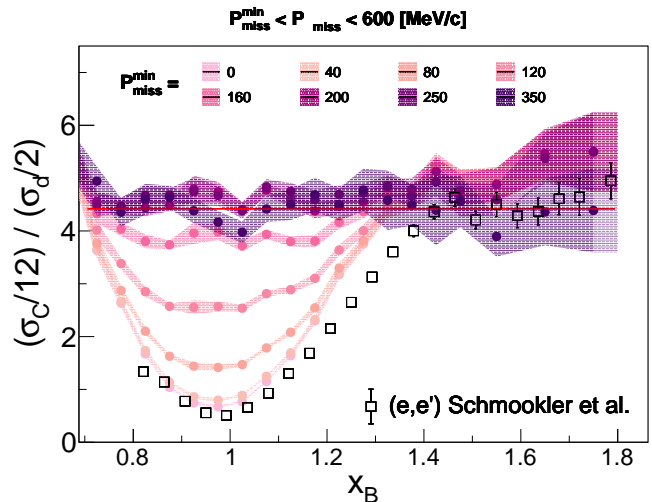


Fig. 1. | **Scaling development in Carbon-to-deuterium $(e, e'p)$ cross-section ratios.** The per-nucleon cross-section ratios for carbon to deuterium as a function of x_B . Full symbols with different colors stand for different lower limits of the missing momentum integration. The upper missing momentum limit is fixed at 600 MeV/c. The colored bands mark the statistical uncertainty of the data at the $\pm 1\sigma$ or 68% confidence. Open squares are the previously measured inclusive (e, e') per nucleon cross-section ratios of Ref. [25]. The horizontal line shows the average (e, e') cross-section ratio for $1.45 \leq x_B \leq 1.8$ [25].

nation of the SRC scaling onset.

This experiment used $|\vec{p}_{miss}|$ to select the approximate initial momentum of the struck nucleon, rather than Q^2 and x_B . We required $Q^2 \geq 1.5 \text{ (GeV}/c)^2$ and, as in previous work [29, 30], we required that the proton be emitted within 25° of the virtual photon.

In order to separate QE and non-QE scattering, we plotted the missing mass, assuming that the electron scattered from a stationary two-nucleon pair:

$$M_{miss}^2 = (\omega + m_d - E_p)^2 - |\vec{q} - \vec{p}_p|^2 \quad (1)$$

where $E_p = \sqrt{|\vec{p}_p|^2 + m^2}$ is the proton energy and m and $m_d \approx 2m$ are the proton and deuteron masses, respectively. In reality, the two-nucleon pair has a binding energy $E_{pair-binding}$ and a non-zero pair center-of-mass momentum $\vec{p}_{c.m.}$, which will broaden the missing mass distribution. The M_{miss} distribution shows a clear peak at the nucleon mass corresponding to QE scattering for all values of x_B from 0.7 to 1.8 (see Extended data Fig. 1). In order to reduce the effects of non-QE scattering, we required $0.8 \leq M_{miss} \leq 1.08 \text{ GeV}/c^2$, i.e. below the pion production threshold. For $0.7 \leq x_B \leq 1.35$ there is a tail extending under the QE peak due to inelastic events. Thus, we need to separate QE scattering from the inelastic backgrounds that extend into the QE peak region at $M_{miss} \leq 1.08 \text{ GeV}/c^2$, especially at low x_B . See Methods for details.

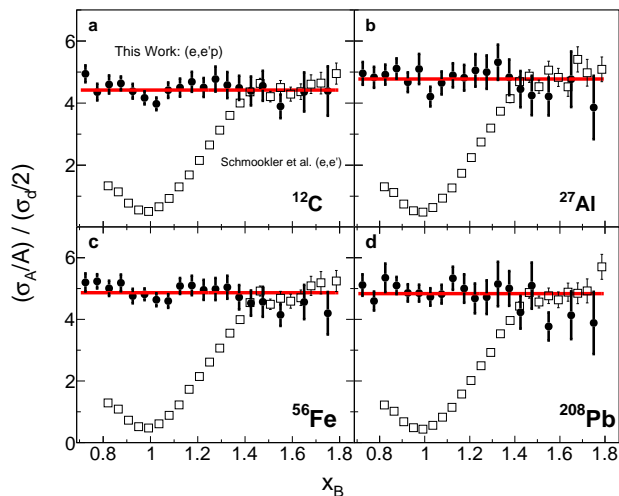


Fig. 2. | **Cross-section Scaling for nuclei from Carbon to Lead.** Measured semi-exclusive $(e, e'p)$ per nucleon cross section ratios for Carbon (a), Aluminum (b), Iron (c) and Lead (d) relative to Deuterium shown as function of x_B and for $350 \leq p_{miss} \leq 600$ MeV/c. Open squares are the previously measured inclusive (e, e') per nucleon cross-section ratios of Ref. [25]. The horizontal lines shows the average (e, e') cross-section ratio for $1.45 \leq x_B \leq 1.8$ [25]. Error bars show the total data uncertainty (statistical + systematical) at the 1σ or 68% confidence.

Such backgrounds are often estimated by fitting the distribution to a gaussian peak and a background. However, because the shape of this background is unconstrained, this would lead to large uncertainties. Instead we follow Ref. [4, 27] and select QE events using $\theta_{\vec{p}_{miss}, \vec{q}}$, the angle between \vec{p}_{miss} and \vec{q} (see Extended Data Fig. 2). In non-QE reactions the momentum transferred to undetected particles shifts the direction of \vec{p}_{miss} and increases $\theta_{\vec{p}_{miss}, \vec{q}}$. We fit the $\theta_{\vec{p}_{miss}, \vec{q}}$ distribution with two gaussians and selected the cut-off angle between the QE and background events as the point where the two gaussians intersected. This procedure included some inelastic events included as QE and excluded some QE events. These errors offset each other. (see dashed histograms in Extended Data Fig. 1).

To test our identification of QE SRC breakup events we examined the width of the resulting missing-mass peak after the $\theta_{\vec{p}_{miss}, \vec{q}}$ cut. The width of this distribution will depend on the CLAS resolution and on the SRC pair c.m. motion. We subtracted the deuterium missing mass peak width (which has no contribution from SRC pair c.m. motion) from that of the heavier nuclei for each x_B bin in order to determine the width due to the pair c.m. motion, $\sigma_{int}^A = \sqrt{(\sigma_{exp}^A)^2 - (\sigma_{exp}^d)^2}$ where σ_{exp} is the measured missing mass distribution width extracted from a Gaussian fit to the data.

The resulting x_B dependence of σ_{int}^C is shown in Fig. 3. It is compared with a calculation using the Generalized

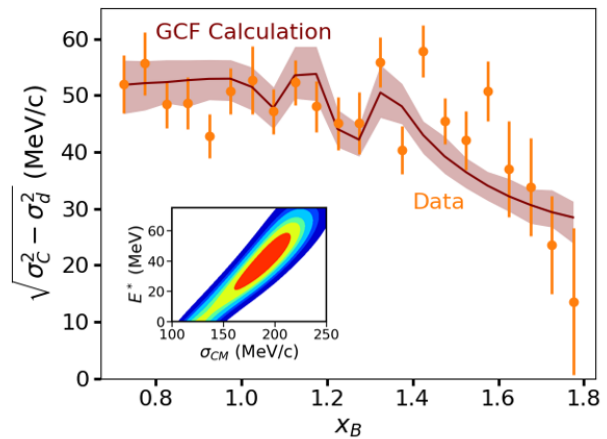


Fig. 3. | **SRC pairs characteristics from $(e, e'p)$ missing mass.** The intrinsic width of the ^{12}C M_{miss} distribution, plotted vs x_B . Orange points show the data. Red curve and error band show a GCF calculation with the SRC pair c.m. momentum distribution width σ_{CM} and the residual $A-2$ system excitation energy E^* fit to the data. Data error bars and calculation error band show the total uncertainty (statistical + systematical) at the 1σ or 68% confidence level. Inset: The resulting confidence intervals of the correlation between the fitted values of σ_{CM} and E^* . The inner region (red) shows the 1σ (68%) confidence region with each region increasing the confidence by an additional 1σ .

Contact Formalism (GCF) [9, 18, 32] that assumes electron scattering from nucleons in SRC pairs with a realistic gaussian c.m. momentum distribution [33], as was done in Ref. [30, 34, 35]. The calculation accounts for the CLAS detector acceptance and resolution and our event selection cuts, see Methods for details. The width of the c.m. momentum distribution σ_{CM} and the excitation energy of the residual nuclear system after the SRC breakup E^* were fitted to the data. The 68% and 90% confidence ranges of the fit values of σ_{CM} of 160–210 and 125–220 MeV/c agree well with previous direct measurements [33, 35]. While E^* was not previously measured, the resulting 68% and 90% confidence ranges of 20–55 MeV and 0–70 MeV are consistent with previous analyses [30]. The reasonableness of the fit parameters and the agreement between the GCF calculation and the data for σ_{int}^C further support our interpretation of the data as dominated by scattering off SRC pairs.

Using the selected event samples, we extracted the $(e, e'p)$ cross-section ratios for scattering off the solid targets relative to deuterium for each bin in x_B . We first divided the ratio of the measured number of events for a given target to deuterium by the ratio of the experimental integrated luminosities to determine the normalized-yield ratios. We then determined the cross-section ratios by correcting the normalized-yield ratios for attenuation of the outgoing protons as they traverse the different nuclei, and for other experimental effects including the small dif-

ference in the CLAS acceptance for detecting particles emitted from the deuterium and the solid targets and electron radiation effects. Acceptance effects were calculated using the CLAS detector simulation [36] and an electron scattering reaction event generator based on the GCF as applied in previous studies [30, 34], see Methods for details.

The extracted per nucleon ($e, e'p$) cross section ratios for Carbon relative to Deuterium are shown in Fig. 1 as a function of x_B for different p_{miss} ranges, varying the lower integration limit from 0 to 350 MeV/c and keeping the upper limit fixed at 600 MeV/c. The curve for $p_{miss}^{min} = 0$ agrees very well with the inclusive data of Schmookler, et al. [25], as expected. The inclusive data show a minimum at $x_B \approx 1$ and a plateau for $x_B \geq 1.5$. As p_{miss}^{min} is increased, the minimum at $x_B = 0$ fills in. For $p_{miss}^{min} \geq 200$ MeV/c, the minimum is completely filled in and the ($e, e'p$) cross-section ratio scales over the full measured x_B range of 0.7 to 1.8.

Fig. 2 shows the per nucleon ($e, e'p$) cross-section ratios for carbon, aluminum, iron, and lead relative to deuterium as a function of x_B and for $350 \leq p_{miss} \leq 600$ MeV/c. The ($e, e'p$) ratios scale for all four nuclei over the entire x_B range, and the cross section ratio is consistent with the inclusive ratios at $x_B \geq 1.5$. The plateau in the ($e, e'p$) cross section ratio extends down to $x_B = 0.7$, far below the inclusive scaling limit of $x_B \approx 1.5$.

Lastly, we quantify the missing momentum where the ($e, e'p$) cross-section ratio scaling begins. Fig. 4 shows the Carbon to Deuterium ($e, e'p$) cross-section ratio integrated over $0.7 \leq x_B \leq 1.8$ as a function of p_{miss} . The high- p_{miss} data is in excellent agreement with a GCF calculation whose parameters were fully determined by *ab-initio* many-body calculations ???. This agreement further supports our identification of QE scattering events and the dominance of scattering from nucleons in SRC pairs at high- p_{miss} .

The cross section ratio becomes flat starting at $p_{miss} \approx 250$ MeV/c. This agrees with the onset of scaling determined from inclusive measurements of 275 ± 25 MeV/c [23] and is slightly larger than the extracted ^{12}C Fermi momentum, $k_F = 220$ MeV/c [37]. However, this onset needs to be quantified.

We quantified the transition and its uncertainties by subtracting the contribution of the mean-field carbon nucleons to the cross-section ratio. We calculated the contribution of the mean-field nucleons to the ^{12}C cross section using a factorized plane-wave impulse approximation with a mean-field spectral function extracted from Quantum Monte-Carlo calculations of the overlap between the ^{12}C and ^{11}B +proton wave functions, see Methods for details. The ratio of this $\text{C}(e, e'p)$ mean-field calculation to the calculated deuterium cross section agrees well with the measured cross section ratios up to $p_{miss} \approx 180$ MeV/c (see Fig. 4).

We then subtracted the mean-field calculation ratio

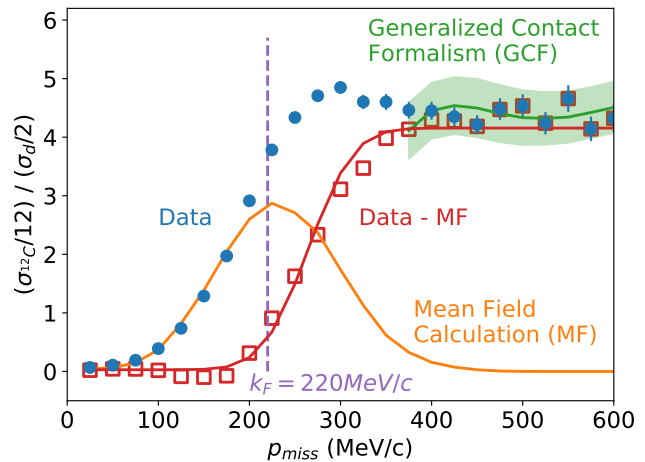


Fig. 4. | Mean field to SRC transition. The per nucleon ($e, e'p$) cross-section ratios for carbon over deuterium as a function of p_{miss} , integrated over $0.7 \leq x_B \leq 1.8$. The filled blue circles show the data; the solid orange line and the green band show the ratios of the calculated cross-sections for mean-field and SRC nucleons in carbon respectively, divided by the measured deuterium data; and the open red squares show the difference between the measured ratios and the mean-field calculation. The solid red line is the result of an erf fit to the open squares. Data error bars and the width of the green band show their total uncertainties (statistical + systematical) at the 1σ or 68% confidence level.

from the data ratio to isolate the contribution from non-mean-field protons (see Fig. 4). The subtracted cross-section ratio matches the profile of a transition function that starts at zero for low- p_{miss} , grows around k_F , and then saturates at high- p_{miss} . We quantified this transition by fitting the subtracted data to an erf function with a fitted transition mean of 258 ± 6 MeV/c and an intrinsic width of 30 ± 6 MeV/c. The intrinsic width is the result of subtracting the contribution of the CLAS resolution from the measured width, see Methods for details.

Thus, the nuclear scaling measurements we present allow isolating interactions with SRCs in a new kinematical regime. By examining the scaling onset and accounting for the mean-field contributions to the data we isolated a new transition function. This function describes the transition from the mean-field to the SRC components of the nucleus. The narrow nature of the transition supports the use of scale-separated models for calculations of nuclear structure and reactions.

* Equal Contribution

† Contact Author (hen@mit.edu)

[1] B. Alex Brown and B. H. Wildenthal. Status of the nuclear shell model. *Ann. Rev. Nucl. Part. Sci.*, 38:29–66, 1988.

- [2] Gerhard Jacob and Th.A.J. Maris. Quasi-Free Scattering and Nuclear Structure. *Rev. Mod. Phys.*, 38:121–142, 1966.
- [3] E. Caurier, G. Martinez-Pinedo, F. Nowacki, A. Poves, and A. P. Zuker. The Shell Model as Unified View of Nuclear Structure. *Rev. Mod. Phys.*, 77:427–488, 2005.
- [4] R. Subedi et al. Probing Cold Dense Nuclear Matter. *Science*, 320:1476–1478, 2008.
- [5] Claudio Ciofi degli Atti. In-medium short-range dynamics of nucleons: Recent theoretical and experimental advances. *Phys. Rept.*, 590:1–85, 2015.
- [6] O. Hen, G. A. Miller, E. Piassetzky, and L. B. Weinstein. Nucleon-Nucleon Correlations, Short-lived Excitations, and the Quarks Within. *Rev. Mod. Phys.*, 89(4):045002, 2017.
- [7] Claudio Ciofi degli Atti and S. Simula. Realistic model of the nucleon spectral function in few and many nucleon systems. *Phys. Rev. C*, 53:1689, 1996.
- [8] H. Feldmeier, W. Horiuchi, T. Neff, and Y. Suzuki. Universality of short-range nucleon-nucleon correlations. *Phys. Rev. C*, 84:054003, 2011.
- [9] R. Cruz-Torres, D. Lonardonì, R. Weiss, N. Barnea, D. W. Higinbotham, E. Piassetzky, A. Schmidt, L. B. Weinstein, R. B. Wiringa, and O. Hen. Many-Body Factorization and Position-Momentum Equivalence of Nuclear Short-Range Correlations. *Nature Physics*, 17:306, 2020.
- [10] E. P. Segarra, J. R. Pybus, F. Hauenstein, D. W. Higinbotham, G. A. Miller, E. Piassetzky, A. Schmidt, M. Strikman, L. B. Weinstein, and O. Hen. Short-Range Correlations and the Nuclear EMC Effect in Deuterium and Helium-3. 6 2020.
- [11] R. Abdul Khalek et al. Science Requirements and Detector Concepts for the Electron-Ion Collider: EIC Yellow Report. 3 2021.
- [12] L. Alvarez-Ruso et al. NuSTEC White Paper: Status and challenges of neutrino–nucleus scattering. *Prog. Part. Nucl. Phys.*, 100:1–68, 2018.
- [13] Leonid Frankfurt and Mark Strikman. Hard nuclear processes and microscopic nuclear structure. *Phys. Rep.*, 160(5-6):235 – 427, 1988.
- [14] S. Paschalis, M. Petri, A. O. Macchiavelli, O. Hen, and E. Piassetzky. Nucleon-nucleon correlations and the single-particle strength in atomic nuclei. *Phys. Lett. B*, 800:135110, 2020.
- [15] L.L. Frankfurt, M.I. Strikman, D.B. Day, and M. Sargsyan. Evidence for short-range correlations from high q^2 (e,e') reactions. *Phys. Rev. C*, 48:2451, 1993.
- [16] O. Hen, Bao-An Li, Wen-Jun Guo, L. B. Weinstein, and Eli Piassetzky. Symmetry energy of nucleonic matter with tensor correlations. *Phys. Rev. C*, 91:025803, Feb 2015.
- [17] Reynier Cruz-Torres, Axel Schmidt, Gerald A. Miller, Lawrence B. Weinstein, Nir Barnea, Ronen Weiss, Eliezer Piassetzky, and O. Hen. Short range correlations and the isospin dependence of nuclear correlation functions. *Phys. Lett.*, B785:304–308, 2018.
- [18] R. Weiss, R. Cruz-Torres, N. Barnea, E. Piassetzky, and O. Hen. The nuclear contacts and short range correlations in nuclei. *Phys. Lett. B*, 780:211, 2018.
- [19] H. Hakobyan et al. A double-target system for precision measurements of nuclear medium effects. *Nucl. Instrum. Meth.*, A592:218–223, 2008.
- [20] B. A. Mecking et al. The CEBAF Large Acceptance Spectrometer (CLAS). *Nucl. Instrum. Meth.*, A503:513–553, 2003.
- [21] M. Duer et al. Probing high-momentum protons and neutrons in neutron-rich nuclei. *Nature*, 560(7720):617–621, 2018.
- [22] K. Egiyan et al. *Phys. Rev. C*, 68:014313, 2003.
- [23] K. Egiyan et al. Measurement of 2- and 3-nucleon short range correlation probabilities in nuclei. *Phys. Rev. Lett.*, 96:082501, 2006.
- [24] N. Fomin et al. New measurements of high-momentum nucleons and short-range structures in nuclei. *Phys. Rev. Lett.*, 108:092502, 2012.
- [25] B. Schmookler et al. Modified structure of protons and neutrons in correlated pairs. *Nature*, 566(7744):354–358, 2019.
- [26] R. Weiss, A. W. Denniston, J. R. Pybus, O. Hen, E. Piassetzky, A. Schmidt, L. B. Weinstein, and N. Barnea. Extracting the number of short-range correlated nucleon pairs from inclusive electron scattering data. *Phys. Rev. C*, 103(3):L031301, 2021.
- [27] R. Shneor et al. Investigation of proton-proton short-range correlations via the $C-12(e, e'$ -prime $pp)$ reaction. *Phys. Rev. Lett.*, 99:072501, 2007.
- [28] I. Korover, N. Muangma, O. Hen, et al. Probing the Repulsive Core of the Nucleon-Nucleon Interaction via the $4He(e, e'pN)$ Triple-Coincidence Reaction. *Phys. Rev. Lett.*, 113:022501, 2014.
- [29] O. Hen et al. Momentum sharing in imbalanced Fermi systems. *Science*, 346:614–617, 2014.
- [30] A. Schmidt et al. Probing the core of the strong nuclear interaction. *Nature*, 578(7796):540–544, 2020.
- [31] R. Cruz-Torres et al. Probing few-body nuclear dynamics via 3H and 3He ($e, e'p$) pn cross-section measurements. *Phys. Rev. Lett.*, 124:212501, 2020.
- [32] Ronen Weiss, Betzalel Bazak, and Nir Barnea. Generalized nuclear contacts and momentum distributions. *Phys. Rev.*, C92(5):054311, 2015.
- [33] E. O. Cohen et al. Center of Mass Motion of Short-Range Correlated Nucleon Pairs studied via the $A(e, e'pp)$ Reaction. *Phys. Rev. Lett.*, 121(9):092501, 2018.
- [34] J.R. Pybus, I. Korover, R. Weiss, A. Schmidt, N. Barnea, D.W. Higinbotham, E. Piassetzky, M. Strikman, L.B. Weinstein, and O. Hen. Generalized contact formalism analysis of the $^4He(e, e'pN)$ reaction. *Phys. Lett. B*, 805:135429, 2020.
- [35] M. Patsyuk et al. Unperturbed inverse kinematics nucleon knockout measurements with a 48 GeV/c carbon beam. 2 2021.
- [36] Elliott Wolin. Clas - geant simulation, 1996.
- [37] E. J. Moniz, I. Sick, R. R. Whitney, J. R. Ficeneç, R. D. Kephart, and W. P. Trower. Nuclear fermi momenta from quasielastic electron scattering. *Phys. Rev. Lett.*, 26:445–448, Feb 1971.
- [38] R. Ent, B. W. Filippone, N. C. R. Makins, R. G. Milner, T. G. O'Neill, and D. A. Wasson. Radiative corrections for (e, e' -prime p) reactions at GeV energies. *Phys. Rev.*, C64:054610, 2001.
- [39] Andreas Aste, Kai Hencken, Jurg Jourdan, Ingo Sick, and Dirk Trautmann. Coulomb corrections for quasielastic (e, e' -prime) scattering: Eikonal approximation. *Nucl. Phys.*, A743:259–282, 2004.

Acknowledgments We acknowledge the efforts of the staff of the Accelerator and Physics Divisions at Jefferson Lab that made this experiment possible. The analy-

sis presented here was carried out as part of the Jefferson Lab Hall B data-mining project supported by the US Department of Energy (DOE). The research was also supported by the National Science Foundation, the Israel Science Foundation, the Pazi Foundation, the Chilean Comisión Nacional de Investigación Científica y Tecnológica, the French Centre National de la Recherche Scientifique and Commissariat à l’Energie Atomique, the French–American Cultural Exchange, the Italian Istituto Nazionale di Fisica Nucleare, the National Research Foundation of Korea, and the UK Science and Technology Facilities Council. Jefferson Science Associates operates the Thomas Jefferson National Accelerator Facility for the DOE, Office of Science, Office of Nuclear Physics under contract DE-AC05-06OR23177.

Author Contributions The CEBAF Large Acceptance Spectrometer was designed and constructed by the CLAS Collaboration and Jefferson Lab. Data acquisition, processing and calibration, Monte Carlo simulations of the detector and data analyses were performed by a large number of CLAS Collaboration members, who also discussed and approved the scientific results. The analysis presented here was performed primarily by I.K with help from A.D. GCF calculations and model systematic uncertainty studies were done by A.D. and A.K with guidance from A.S. and J.R.P. Mean-field spectral function calculations were done by A.L and N.R. O.H., A.S., E. Piasetzky, and L.B.W. guided and supervised the analysis.

Competing interests The authors declare no competing interests.

Data Availability The raw data from this experiment are archived in Jefferson Lab’s mass storage silo.

Author Information Reprints and permissions information is available at www.nature.com/reprints. Readers are welcome to comment on the online version of the paper. Publisher’s note: Springer Nature remains neutral with regard to jurisdictional claims in published maps and institutional affiliations. Correspondence and requests for materials should be addressed to O.H. (hen@mit.edu).

Full Author List

xxxx TBD xxxx

Methods

CLAS detector and particle identification. The CEBAF Large Acceptance Spectrometer (CLAS) was based on a toroidal magnetic field and had six independent sectors separated by its magnet coils [20]. Each sector included three layers of drift chambers for charged particle momentum and charge determination, and time-of-flight scintillation counters, Cerenkov counters, and electromagnetic calorimeters for particle identification. The in-plane scattering angle coverage of the drift chambers and time-of-flight scintillation extended from about 8° to 140° , while that of the Cerenkov counters and electromagnetic calorimeters was more limited, extending from about 8° to 45° . The six sectors collectively covered 50 – 80% of the out-of-plane angle (depending on the in-plane scattering angle).

Electrons were distinguished from pions by their large signal in the Cerenkov counters, as well as by a large energy deposition in the electromagnetic calorimeters relative to their momentum. Protons were identified by requiring that their time of flight, measured by the scintillation counters, was consistent to within two standard deviations of the timing measurement resolution, with the calculated time of flight based on the momentum reconstructed in the drift chambers. We applied separate fiducial cuts for electrons and protons to select momentum-dependent regions of CLAS where the detection efficiency was constant and close to one.

We used a specialized dual target setup intended to enable precise extractions of A/d cross-section ratios [19]. The target consisted of a 2 cm long liquid deuterium target, held inside a thin aluminum cell, followed by a thin solid foil of C, Al, Fe, or Pb. The solid foil was placed 4 cm from the end of the liquid-deuterium cell, which was more than enough to unambiguously identify which particles originated from the electron interaction with the liquid deuterium and which from the solid target foil. For each event the measured electron and proton vertices along the beam direction were required to agree to within 0.8 cm, which corresponds to about two standard deviations of the vertex reconstruction resolution.

($e, e'p$) Event Selection. We required $Q^2 > 1.5$ (GeV/c)² and $\theta_{pq} \leq 25^\circ$, that the knocked-out proton was detected within a 25° cone of the momentum transfer vector, \vec{q} . Rather than cutting on the missing-mass to select QE contributions and reject inelastic events, we used a loose missing-mass cut and an x_B -dependent cut on $\theta_{\vec{p}_{miss}, \vec{q}}$, the angle between \vec{p}_{miss} and \vec{q} .

Extended Data Fig. 1 shows the measured M_{miss} (see Eq. 1) distribution for $^{12}\text{C}(e, e'p)$ events for different bins of x_B . There is a peak at the nucleon mass due to quasielastic proton knockout and there is a background at larger missing mass due to inelastic scattering from nucleons resulting in meson production. At high- x_B , where

most previous measurements were done, only QE events are seen, as expected. We cut on $M_{miss} \leq 1.08$ GeV/c^2 , corresponding to about $m + m_\pi$ (where m_π is the pion mass), to suppress most inelastic contributions. However, inelastic events extend to lower missing mass and cannot be cleanly separated by a simple cut on M_{miss} . Since the functional form of the inelastic background is not known, fitting the background would lead to very large uncertainties.

Therefore we adopted the method of Ref. [4, 27] and used $\theta_{\vec{p}_{miss}, \vec{q}}$, the angle between \vec{p}_{miss} and \vec{q} , to separate QE and inelastic events (see Extended Data Fig. 2). In contrast to the missing-mass spectra, $\theta_{\vec{p}_{miss}, \vec{q}}$ is well described by a two-gaussian fit. We chose to cut at the intersection of the two gaussians in order to suppress the vast majority of the inelastic events while keeping most of the QE ones. The remaining fractional contribution of the inelastic events in the QE region is similar in both the heavy nuclei and the deuterium spectra and therefore largely cancels in their ratios.

The effect of the $\theta_{\vec{p}_{miss}, \vec{q}}$ cut on the missing mass distribution is shown in Extended Data Fig. 1 where the dashed histograms show the missing-mass distributions separately for events above and below the cut. This cut thus identifies the inelastic tail that extends into the QE region. The small- $\theta_{\vec{p}_{miss}, \vec{q}}$ events in the M_{miss} distribution are well described by a gaussian. This is an encouraging observation that shows that our procedure results in similar performance to those of the traditional peak+background fit procedure, but using well defined kinematical cuts that are suitable for QE scattering studies and allow for direct comparison with theoretical calculations.

We varied the $\theta_{\vec{p}_{miss}, \vec{q}}$ cut to show that our results are not sensitive to specific method of removing the inelastic contributions (see Extended Data Fig. 3). Varying the angular cut by $\pm 5^\circ$ and even removing it entirely did not significantly change the cross-section ratios. This shows that the effect of the residual inelastic contributions cancels in the cross-section ratio.

The systematic uncertainties associated with the inelastic suppression procedure specifically, and our event selection cuts more broadly, are discussed in the following sections.

Cross-section extraction. The reported per-nucleon cross-section ratios are extracted from the measured number of ($e, e'p$) events originating from the solid and liquid-deuterium targets by normalizing them by the integrated measured per-nucleon luminosity, and applying corrections for experimental effects such as acceptance and electron radiative effects, as well as for nucleon attenuation effects. The general expression for the per-nucleon ($e, e'p$) A/d cross-section ratio for a given x_B bin is given

by:

$$\frac{\sigma_A/A}{\sigma_d/2}(x_B) = \frac{Y_{(e,e'p)}^A(x_B)}{Y_{(e,e'p)}^d(x_B)} \times Acc_{A/d}(x_B) \times RC_{A/d}(x_B) \times \frac{T_d}{T_A}, \quad (2)$$

where $Y_{(e,e'p)}^A(x_B)$ and $Y_{(e,e'p)}^d(x_B)$ are the luminosity-normalized measured number of $(e, e'p)$ events from target A or d respectively in a given x_B bin, $Acc_{A/d}(x_B)$ is the relative acceptance of the CLAS detector for $(e, e'p)$ events originating from the solid foil target relative to those from the liquid deuterium target, $RC_{A/d}(x_B)$ is the ratio of the nucleus A and d radiative correction factors, and T_A and T_d are transparency factors accounting for the attenuation of nucleons as they exit nucleus A or nucleus d .

To determine the deuteron event yield, $Y_{(e,e'p)}^d(x_B)$, we separated events originating from interactions with deuterium nuclei and with the aluminum end caps of the target cell. We minimized the end cap contributions by only considering events with an interaction vertex reconstructed to within the central 1 cm of the 2-cm liquid target. We then used measurements with an empty target cell to estimate the remaining cell wall contributions. These contributions were independent of x_B and less than 2% of the measured event yield. We thus reduced the measured yield by 2% and accounted for the uncertainty in this subtraction in our systematic uncertainties.

Acceptance Corrections. We corrected the cross section ratio for the slightly different experimental acceptances for events originating in the 2-cm liquid deuterium target and events originating in the solid target foil located 5-cm downstream from the liquid target center. This factor should be small because the target separation is much smaller than the distances from the targets to the detectors. We estimated this correction factor using a Geant simulation of CLAS [36]. We generated separate acceptance maps for electrons and for protons originating from a solid target or from the liquid target as a function of particle momentum and in- and out-of-plane scattering angles. We then used the acceptance maps to calculate the acceptance probability for each experimental event as follows. For each event, we rotated the entire event (both electron and proton) by a random angle ϕ around the beamline and then rotated the proton momentum by a random angle ϕ' around \vec{q} . We then used the acceptance maps to determine the probability that the rotated event, which has approximately the same cross-section as the measured event, would have been detected by CLAS. We did this calculation separately for events from the liquid and solid targets, accounting for the target position when constructing the acceptance maps. This procedure was repeated 100 times for each event. The acceptance weight for that event equalled 100 divided by the total probability that each of those 100 rotated events would have been detected. The average acceptance weight as a function of x_B for each target is

shown in Fig. 4(a). We then took the ratios between the solid- and liquid-target acceptance weights to determine $Acc_{A/d}(x_B)$, the cross-sections-ratio acceptance-correction factor for each x_B -bin (see Fig. 4). The uncertainties in $Acc_{A/d}(x_B)$ were added in quadrature to the point-to-point statistical uncertainties of the data.

Radiative and coulomb effects. The radiative correction factors were by calculating the ratio between the Born cross-section and the cross-section including electron-radiative effects. The latter uses the peaking approximation [38] as implemented in by Ref. [34]. The cross sections for the solid targets were calculated using the GCF model and the deuteron cross sections were calculated with **add info here**

As part of modified electron kinematics, we also used the Effective Momentum Approximation [39] to account for Coulomb effects that accelerate the incoming electron and knockout proton and decelerate the scattered electron by an energy ΔE , see Ref. [34] for details. We used ΔE values of 0, 2.9, 5.6, 9.4 and 20.3 MeV for d , C, Al, Fe and Pb targets, respectively.

The resulting radiative correction factors, $RC_{A/d}(x_B)$, are shown in Extended Data Fig. 5.

Transparency Corrections. After the electron scatters from a proton, the proton needs to travel through the residual nucleus to be detected. If the proton rescatters too much from the other nucleons, then it will fall outside our event acceptance cuts. The probability of the proton to be detectable after exiting from nucleus depends on the size of the nucleus. The nuclear transparency probabilities were calculated within a Glauber approximation using an effective scattering cross section. The probability that a proton escapes the nucleus without further interaction is given by:

$$T_A = \frac{1}{A} \int d^3r \rho(r) \exp \left[-\sigma_{eff} \int \rho(z) dz \right] \quad (3)$$

where $\rho(r)$ is the nuclear density distribution (assumed symmetrical), $\rho(z)$ is the nuclear density along the path of the exiting proton, and σ_{eff} is the effective nucleon-nucleon cross section. For the 1 – 3 GeV/c protons in this analysis, $\sigma_{eff} = 37 \pm 7$ mb. This gives nuclear transparencies T_A of $1, 0.53 \pm 0.05, 0.43 \pm 0.05, 0.34 \pm 0.04$ and 0.22 ± 0.03 for d, C, Al, Fe and Pb respectively.

Theoretical cross-section calculations. The $(e, e'p)$ nucleon-knockout cross-section for high- Q^2 reactions is modeled here using a factorized plane wave impulse approximation (PWIA) []:

$$\frac{d\sigma_{A(e,e'p)}}{d\Omega_{k'} dE_{k'} d\Omega_p dE_p} = p E_p \sigma_{ep} S_A^N(p_{miss}, E_{miss}), \quad (4)$$

where $(\vec{k}', E_{k'})$ is the scattered electron four-momentum, σ_{ep} is the off-shell electron-nucleon cross-section, and

$S_A^N(p_{miss}, E_{miss})$ is the nuclear spectral function for nucleus A , which defines the probability for finding a nucleon in the nucleus with momentum p_{miss} and energy E_{miss} .

We considered two models for the spectral function, for the mean-field and for the SRC region. The carbon mean-field spectral function is obtained from variational monte-carlo calculation of the overlap between the ^{12}C and the $^{11}\text{B}+p$ wave functions. Each of the ab-initio ^{12}C and ^{11}B wave functions result from the full solution of the many-body problem with two- and three-nucleon forces (using the AV18 and *xxx* two- and three-nucleon interaction models). Therefore, the resulting mean-field spectral function already accounts for the reduced occupancy of mean-field states due to multi-nucleon correlations.

The SRC spectral function for C, Al, Fe and Pb was modeled using the GCF model [1] following the implementation of Ref. [2] with the AV – 18 two-nucleon interaction, using pair center-of-mass motion width of 150 ± 20 MeV/c, and an $A - 2$ excitation energy of $0 - 30$ MeV. The contacts (the probability of finding an SRC pair) were taken from [3].

The complete deuterium spectral function was calculated exactly using the AV18 nucleon-nucleon interaction [4].

The calculated cross-sections were integrated over the CLAS experimental acceptance, using the same event selection cuts as the data, and smeared to account for the CLAS experimental resolution.

Systematic Uncertainties. There were several sources of systematic uncertainties, including both point-to-point and correlated uncertainties.

Coulomb correction: There is a 10% uncertainty in the coulomb potential (ΔE) used for the coulomb correction described above. Varying ΔE by $\pm 10\%$ changed the extracted cross-section ratios by a maximum of 3% (for lead). We conservatively chose to use 3% as the systematic uncertainty due to coulomb correction for all targets and all bins.

Event Selection: We varied each of the event selection cuts within reasonable limits (see Extended Data Table 1) to see the effect of these cuts on the resulting cross-section ratios. We repeated the analysis 100 times, choosing the value of each selection cut randomly from a Gaussian distribution centered at the nominal value with a width reflecting a reasonable variation of the cut. We used the mean and variance in the resulting distribution of 100 cross-section ratios to define the value of cross-section ratio and its event selection cut uncertainty, respectively. These bin-dependent uncertainties ranged from 4.5% to 12.5%.

Transparency: The largest correlated systematic uncertainty is due to the transparency correction. It is driven by the uncertainties in the effective nucleon scattering cross sections used for the Glauber calculations that re-

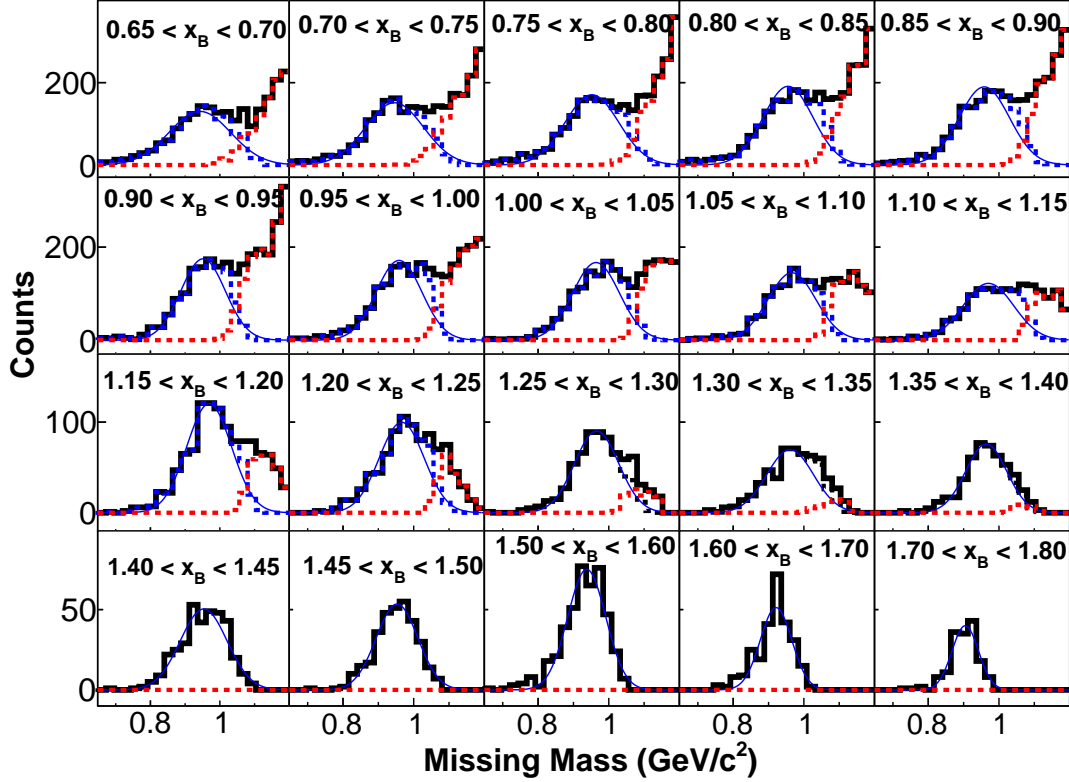
sult in 10% (for carbon) to 15% (for lead) uncertainties in the ratios of transparencies of the solid target nuclei to deuterium, see Ref. [29].

Combining different deuteron run periods: We measured electron scattering from deuterium and from each solid target simultaneously. In order to increase the deuterium statistics, we combined the deuterium data from all of the solid target runs. This reduced the statistical uncertainty of the cross-section ratios but introduced a systematic uncertainty due to the stability of the beam charge measurement that does not fully cancel in the A/d cross-section ratio. This uncertainty was estimated as half of the difference between total averaged and the individual deuteron normalized yields. The maximum difference was 1.5%, which we used as an overall systematic uncertainty.

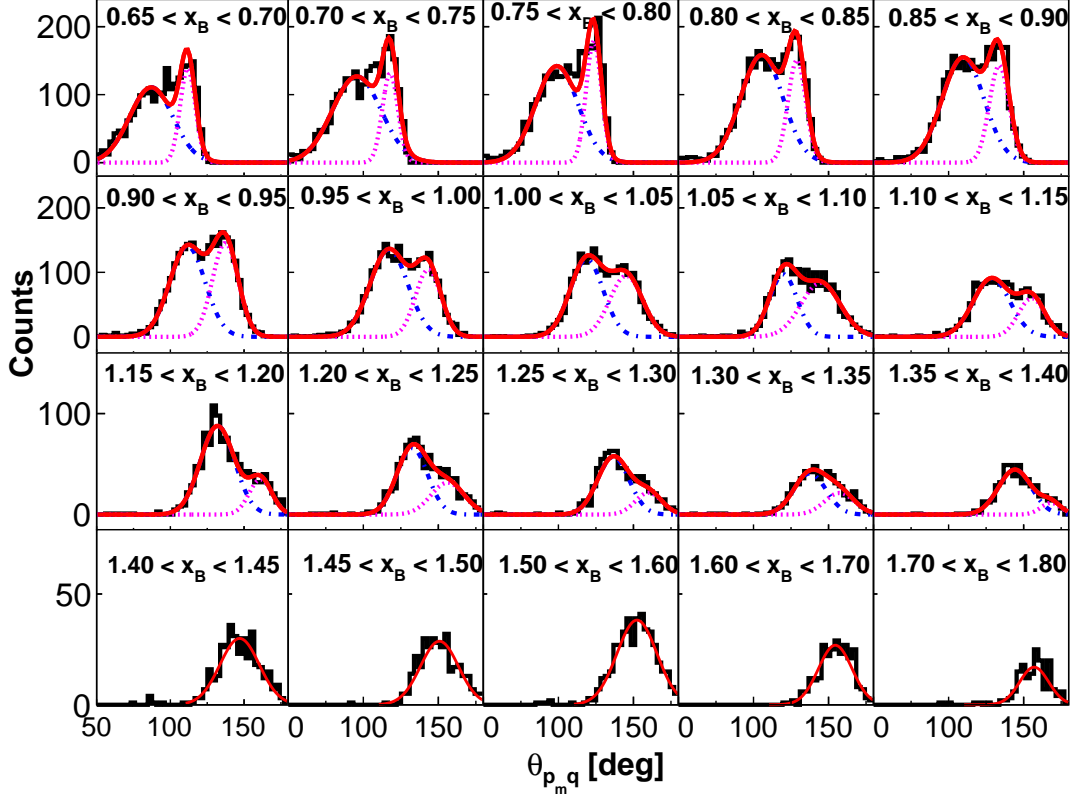
Extended Data Table I. Event selection cut ranges

Cut Type	Nominal Value	1σ
p_{miss} minimum [GeV/c]	0.3	0.015
p_{miss} maximum [GeV/c]	0.6	0.015
M_{miss} minimum [GeV/c ²]	0.8	0.05
M_{miss} maximum [GeV/c ²]	1.08	0.05
θ_{pq}	25°	0.5°
Q^2 [(GeV/c) ²]	1.5	0.01

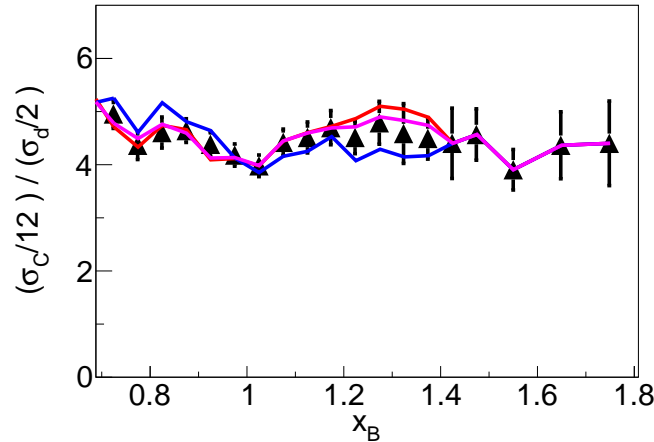
Extended Data



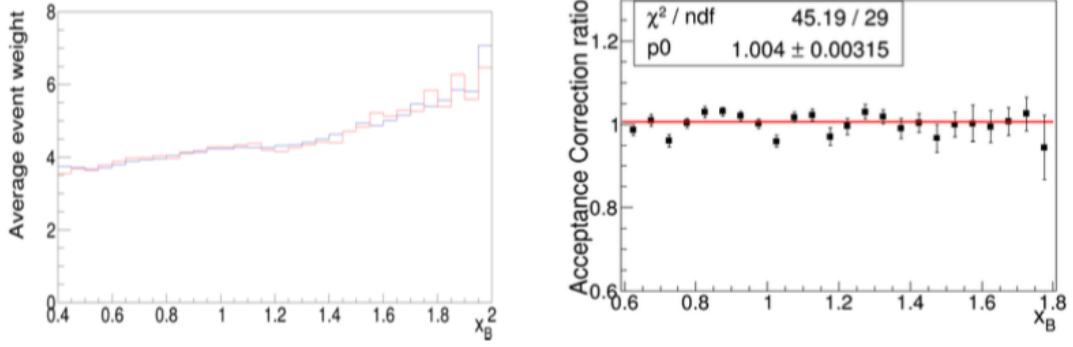
Extended Data Fig. 1. | Missing Mass distributions. Number of events plotted vs M_{miss} for the $C(e, e'p)$ reaction for different bins of x_B . The black histogram represents all events. The blue dashed histogram shows the data cut on $\theta_{\vec{p}_{miss}, \vec{q}}$, the opening angle between the missing momentum \vec{p}_{miss} and the virtual photon \vec{q} , as determined in Extended Data Fig. 2. The red dashed histogram shows the events failing the $\theta_{\vec{p}_{miss}, \vec{q}}$ cut. The thin solid blue line shows the Gaussian fit to the blue dashed histogram.



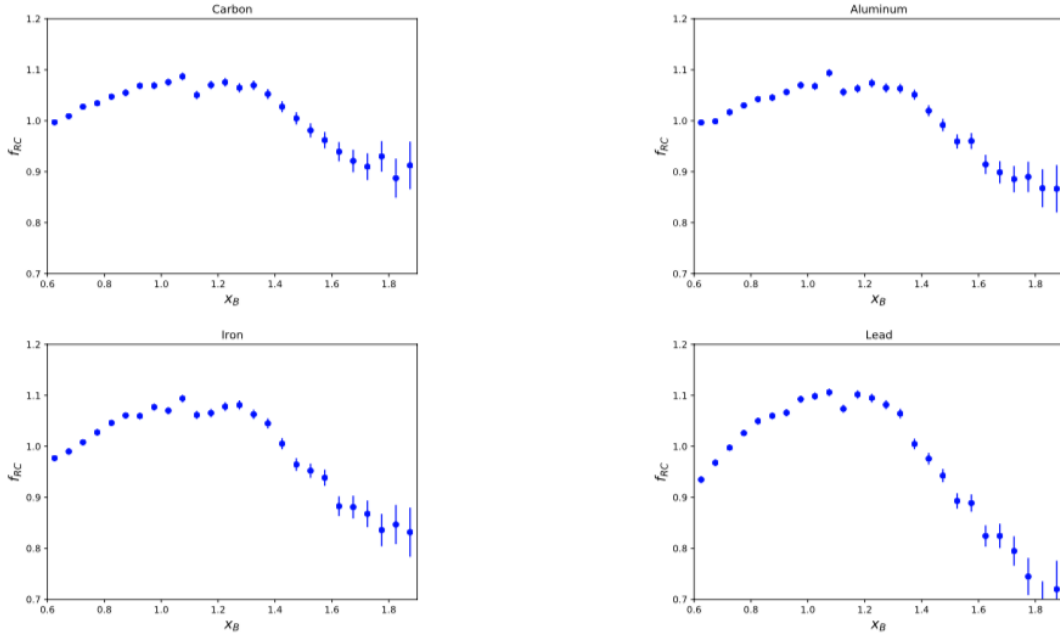
Extended Data Fig. 2. | Opening angle between the missing momentum and the virtual photon. The number of $C(e, e'p)$ events plotted versus $\theta_{\vec{p}_{miss}, \vec{q}}$, the opening angle between \vec{p}_{miss} and \vec{q} , for different bins in x_B . The black histogram shows all events, the blue dot-dashed curve and the magenta dotted curves show the gaussian fits to the two peaks and the total is shown by the solid red line. The intersection of the two gaussians is used as the angular cut for the dashed histograms in Extended Data Fig. 1. At $x_B \geq 1.4$ only one gaussian is fit to the data because the inelastic contribution is negligible.



Extended Data Fig. 3. | Angle cut sensitivity. Measured per-nucleon cross-section ratios for Carbon to Deuterium with different cuts on $\theta_{\vec{p}_{miss}, \vec{q}}$. Black points correspond to nominal cut values, the purple and blue lines show the effect of increasing or decreasing the cut by 5° respectively, and the red line shows the effect of not applying any $\theta_{\vec{p}_{miss}, \vec{q}}$ cut.



Extended Data Fig. 4. | Acceptance Correction. (left) The average acceptance weight for $(e, e'p)$ events from solid (blue histogram) and deuterium (red histogram) targets as a function of x_B and (right) the acceptance correction factors for the cross section ratios, i.e., the ratio of deuterium- to solid-target acceptance-correction weights, as a function of x_B . Points show the data and the error bars show the 1σ or 68% confidence limits. The red line shows a constant fit to the data.



Extended Data Fig. 5. | Radiative and Coulomb Corrections. The combined radiative and Coulomb corrections, $RC_{A/d}(x_B)$, for $(e, e'p)$ events for nucleus A relative to the deuteron for (a) carbon, (b) aluminum, (c) iron and (d) lead. The points show the correction factors and the error bars show the 1σ or 68% confidence limits.